RMetS
Royal Meteorological Society

A dynamical framework for the origin of the diagonal South Pacific and South Atlantic Convergence Zones

Karin van der Wiel,[a,b]* Adrian J. Matthews,[a,b,c] David P. Stevens[a,c] and Manoj M. Joshi[a,b,d]

[a]*Centre for Ocean and Atmospheric Sciences, University of East Anglia, Norwich, UK*
[b]*School of Environmental Sciences, University of East Anglia, Norwich, UK*
[c]*School of Mathematics, University of East Anglia, Norwich, UK*
[d]*Climatic Research Unit, University of East Anglia, Norwich, UK*

*Correspondence to: K. van der Wiel, School of Environmental Sciences, University of East Anglia, Norwich Research Park, Norwich NR4 7TJ, UK. E-mail: k.van-der-wiel@uea.ac.uk

The South Pacific Convergence Zone (SPCZ) and South Atlantic Convergence Zone (SACZ) are diagonal bands of precipitation that extend from the Equator southeastward into the Southern Hemisphere over the western Pacific and Atlantic Oceans, respectively. With mean precipitation rates over 5 mm day^{-1}, they are a major component of the tropical and global climate in austral summer. However, their basic formation mechanism is not fully understood. Here, a conceptual framework for the diagonal convergence zones is developed, based on calculations of the vorticity budget from reanalysis and Rossby wave theory.

Wave trains propagate eastward along the Southern Hemisphere subtropical jet, with initially quasi-circular vorticity centres. In the zonally sheared environment on the equatorward flank of the jet, these vorticity centres become elongated and develop a northwest–southeast tilt. Ray-tracing diagnostics in a non-divergent, barotropic Rossby wave framework then explain the observed equatorward propagation of these diagonal vorticity structures toward the westerly ducts over the equatorial Pacific and Atlantic. The baroclinic component of these circulations leads to destabilisation and ascent ahead of the cyclonic vorticity anomaly in the wave, triggering deep convection because of the high sea surface temperatures in this region. Latent heat release then forces additional ascent and strong upper-tropospheric divergence, with an associated anticyclonic vorticity tendency. A vorticity budget shows that this cancels out the advective cyclonic vorticity tendency in the wave train over the SPCZ, and dissipates the wave within a day. The mean SPCZ is consequently comprised of the sum of these pulses of diagonal bands of precipitation.

Similar mechanisms also operate in the SACZ. However, the vorticity anomalies in the wave trains are stronger, and the precipitation and negative feedback from the divergence and anticyclonic vorticity tendency are weaker, resulting in continued propagation of the wave and a more diffuse diagonal convergence zone.

Key Words: SPCZ; SACZ; tropical–extratropical interaction; Rossby waves

Received 15 September 2014; Revised 5 December 2014; Accepted 15 December 2014; Published online in Wiley Online Library 17 February 2015

1. Introduction

During austral summer, precipitation in the Southern Hemisphere is organised in three large-scale diagonal bands: the South Pacific Convergence Zone (SPCZ), the South Atlantic Convergence Zone (SACZ) and the less significant South Indian Convergence Zone (SICZ) (Figure 1(a)). By contrast, in the Northern Hemisphere there are no such diagonal bands of rainfall; in their place is the zonal Intertropical Convergence Zone (ITCZ). The SPCZ stretches diagonally from New Guinea in the equatorial warm pool to approximately 30°S, 120°W. At its tropical boundary, the SPCZ becomes more zonal and joins the ITCZ over the Indian Ocean (Vincent, 1994). The SACZ extends from the Amazon, over southern Brazil towards the western South Atlantic (Todd *et al.*, 2003). The SICZ over southern Africa and Madagascar is less distinct than the SPCZ and SACZ and does not extend as far into the midlatitudes. Even though it has been linked to large-scale circulation patterns and convergence (Cook, 2000), the focus here will mainly be on the SPCZ and SACZ.

Though the SPCZ lies mostly over the South Pacific Ocean, there are many small island states that depend on its rainfall (e.g. Griffiths *et al.*, 2003; Kumar *et al.*, 2006). Small displacements

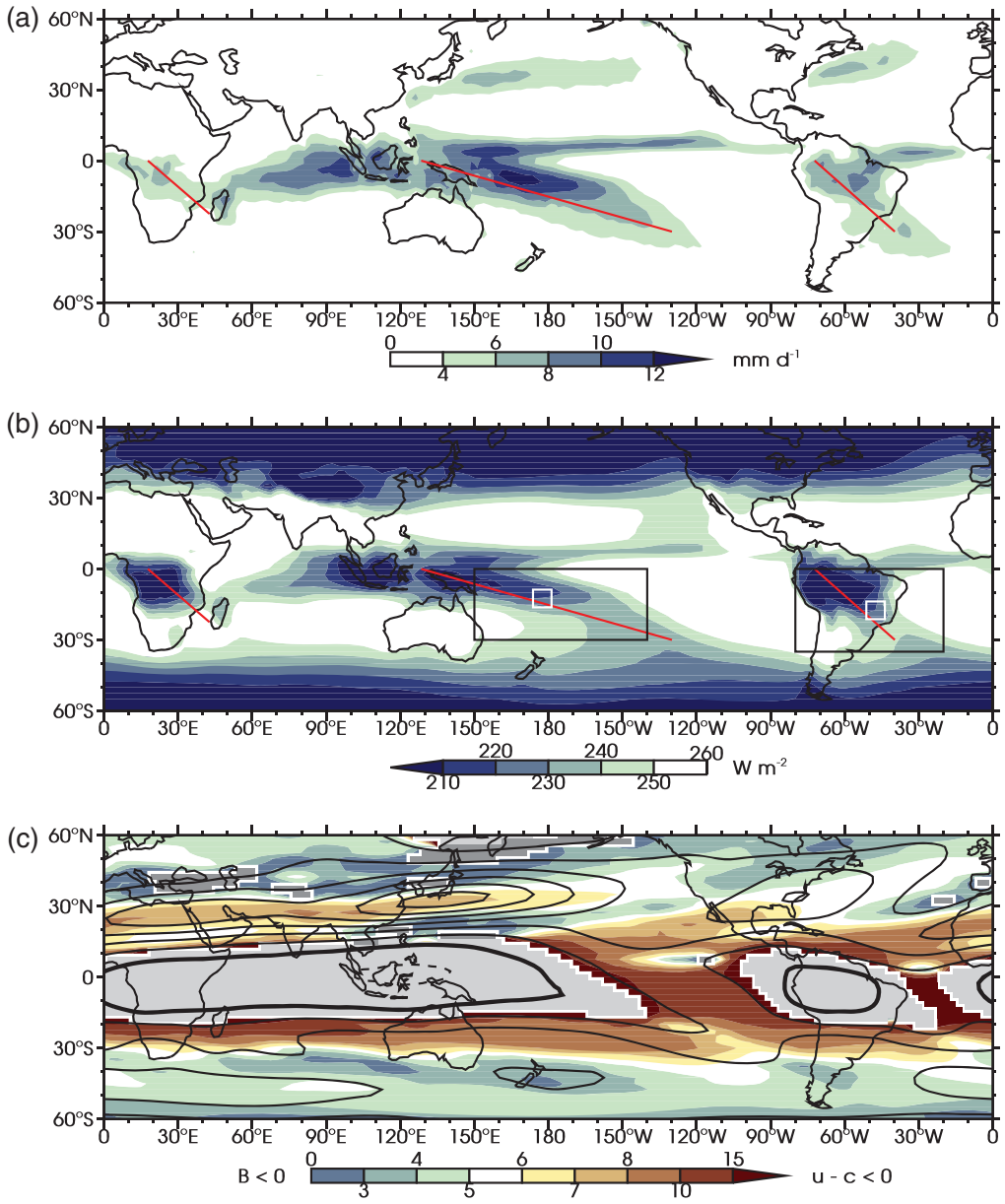

Figure 1. November to April time mean of (a) precipitation rate (mm day^{-1}, data source: CMAP), (b) OLR (W m^{-2}, data source: Interpolated OLR Dataset) and (c) 200 hPa zonal total wavenumber for Rossby waves of phase speed 6 m s^{-1} in shaded colours (data source: NCEP-DOE reanalysis). Grey/red diagonal lines in (a) and (b) indicate the position of the mean convection axis of the SPCZ, the SACZ and the SICZ. Small grey boxes in (b) indicate the areas of the power spectra in Figure 2, large black boxes indicate the areas of the EOF analyses in Figure 3. Contours in (c) show 200 hPa zonal wind (10 m s^{-1} contour interval, negative contours dashed, zero contour thickened). Light grey shading in (c) corresponds to areas of $(\overline{u} - c) < 0$, dark grey shading to $\hat{\beta} < 0$.

in its location have resulted in severe droughts and floods across the region (Cai *et al.*, 2012). Understanding the processes that set the SPCZ location and cause its temporal variability is therefore crucial for the inhabitants of these island states. The SPCZ varies on intraseasonal time-scales through the influence of the Madden–Julian Oscillation (MJO; Matthews *et al.*, 1996; Matthews, 2012; Haffke and Magnusdottir, 2013), on interannual time-scales with El Niño-Southern Oscillation (ENSO; Matthews, 2012; Haffke and Magnusdottir, 2013; Murphy *et al.*, 2014) and on interdecadal time-scales (Salinger *et al.*, 2001; Folland *et al.*, 2002). Furthermore, both SPCZ and SACZ have a strong influence on Southern Hemisphere weather and climate. For example, the SPCZ is one of the main sources of lightning activity in the region away from the land (Ortéga and Guignes, 2007) and a location favourable for tropical cyclone development (Vincent *et al.*, 2011). The SACZ plays a role in the onset of the South American monsoon (Nieto Ferreira *et al.*, 2011).

The diagonal rainfall patterns were first observed during the early days of satellite data (Hubert, 1961; Streten, 1973) and were linked to tropical–extratropical interactions. Trenberth (1976) noted that Rossby waves end their life-cycle in the SPCZ area and called it a 'graveyard region for fronts moving from the southwest'. Modelling experiments have shown there is limited influence of the Southern Hemisphere continental distribution on the SPCZ (Kiladis *et al.*, 1989), though orography has been found to influence the location of the northeastern edge of the SPCZ (Takahashi and Battisti, 2007; Lintner and Neelin, 2008). Kodama (1992, 1993) compared the SPCZ and SACZ. Common features included the fact that both zones were anchored to an equatorial deep convection area and both were found in the vicinity of a subtropical jet. Disturbances from these jets play an important role in creating SPCZ and SACZ convection; the accumulation of wave energy in the jet exit ($\partial\overline{u}/\partial x < 0$) has been linked to their diagonal orientation (Widlansky *et al.*, 2011).

Midlatitude influence on the Tropics is mainly through Rossby waves propagating equatorward. Following the conceptual framework of Meehl *et al.* (2001), synoptic Rossby waves propagate on the atmospheric mean state that is set by processes on interannual and intraseasonal time-scales (e.g. ENSO and the MJO). Eastward-propagating Rossby waves ($\omega > 0$, $c > 0$) are limited to areas where $(\overline{u} - c) > 0$ (Yang and Hoskins, 1996); in areas of mean westerly flow, stationary Rossby waves ($c = 0$) can

freely propagate. These waves propagate through jet regions that act as wave guides and are refracted towards latitudes with higher zonal total wavenumber

$$K_\omega = \left(\frac{\hat{\beta}_M}{\overline{u}_M - c} \right)^{1/2}, \quad (1)$$

where $\hat{\beta}$ is the meridional gradient of absolute vorticity, $\overline{u}$ is the zonal wind, c is the zonal phase speed and subscript M denotes a Mercator projection (Karoly, 1983; Hoskins and Ambrizzi, 1993). Figure 1(c) shows the November to April time mean geographical distribution of K_ω at 200 hPa for Rossby waves with a typical phase speed of 6 m s^{-1}. Rossby waves from the subtropical jet are refracted equatorward towards the westerly winds over the eastern equatorial Pacific. This 'westerly duct' allows for cross-equatorial Rossby wave propagation (Webster and Holton, 1982). Rossby waves from the jet southwest of Australia pass over the SPCZ area; Rossby waves refracting towards the westerly duct in the equatorial Atlantic pass over the SACZ area. During austral winter, the westerly ducts disappear and equatorward refraction of midlatitude Rossby waves stops (Ambrizzi *et al.*, 1995); coincidentally the SPCZ and SACZ are much less pronounced.

These Rossby waves can directly trigger convection over the SPCZ and SACZ regions. Poleward flow ahead of cyclonic anomaly centres in the waves is associated with ascent and decreased static stability according to quasi-geostrophic dynamics. The Tropics are sensitive to such forcing (high sea surface temperatures, conditionally unstable atmospheric conditions) and deep convection and precipitation can be triggered. Observational analysis has shown that transient convection in the ITCZ during austral summer can be explained by this sequence of events (Kiladis and Weickmann, 1992a, 1992b Kiladis, 1998). Aquaplanet experiments have demonstrated the importance of equatorward propagating midlatitude disturbances in setting up a diagonal rainfall band (Nieto Ferreira and Chao, 2013). In the SACZ region a similar configuration of upper-tropospheric Rossby wave and convection is found (Liebmann *et al.*, 1999; Robertson and Mechoso, 2000). Besides their influence on tropical convection, these Rossby waves have an important role in setting the momentum balance of the atmosphere (Kiladis, 1998).

For the SPCZ area, the Rossby wave forcing of convection following the mechanism described above is discussed by Matthews (2012). It is noted that the wave decays within a day after convection is triggered. A hypothesis is proposed of a possible link and negative feedback between the convection and precipitation triggered by the transient wave and the subsequent decay of the wave. The diabatic heating released from condensation associated with the anomalous convection is substantial. This heating forces extra ascent and upper-tropospheric divergence. The divergence is a source of anticyclonic vorticity (vortex stretching, $\partial\zeta/\partial t = -fD$, where ζ is relative vorticity, t is time, f is the planetary vorticity and D is horizontal divergence). By means of a scale analysis, it is shown that this anticyclonic vorticity tendency is large enough to remove the cyclone in the transient wave and dissipate the wave.

In this article, observation-based data will be used to investigate the diagonal orientation of both convergence zones. The analysis of Matthews (2012) will be extended with a full vorticity budget, which quantifies the strength of the proposed negative feedback mechanism. Rossby ray-tracing techniques will be used to investigate Rossby wave propagation in the region. The analysis will be repeated for the SACZ. In the next section, all data products that are used will be discussed. In section 3 we investigate temporal and spatial variability patterns for both regions. In section 4 the temporal evolution of transient waves are discussed. A framework for the diagonal SACZ is presented in section 5, followed by a framework for the diagonal SPCZ in section 6. The results are summarized in section 7 together with a discussion of their implications for global climate.

2. Data

In tropical regions where precipitation is mostly from deep convection, outgoing long-wave radiation (OLR) can be used as a proxy for precipitation (e.g. Lau and Chan, 1983; Janowiak and Arkin, 1991; Xie and Arkin, 1998). The annual cycle of temperature is small, therefore the strongest variations of OLR are the result of the presence of deep convective clouds (Salby, 2012). Figure 1(a,b) show time mean patterns of precipitation and OLR, respectively. In the Tropics (approximately 30°S–30°N) more negative OLR values correspond to enhanced convection and more positive precipitation values; the SPCZ, SACZ and ITCZ can be identified in both panels. Higher OLR values are associated with reduced convection and negative precipitation anomalies, e.g. over the east Pacific dry zone. Polewards of 30°S/N, OLR decreases due to decreasing surface and atmospheric temperatures.

For OLR, the Interpolated OLR Dataset is used. These are estimates from the NOAA/NESDIS* polar-orbiting satellites providing space and time interpolated data; the interpolation algorithm is described by Liebmann and Smith (1996). Data used are daily means from 1979 to 2013 on a 2.5° × 2.5° grid.

Additionally, precipitation data from the Climate Prediction Center Merged Analysis of Precipitation (CMAP) project are used (Xie and Arkin, 1997). This is a precipitation product based on gauge observations from the Global Precipitation Climatology Center (GPCC, Rudolf *et al.*, 1994), five different satellite-based precipitation estimates and the NCEP–NCAR† reanalysis (Kalnay *et al.*, 1996). The satellite estimates included are the Geostationary Operational Environmental Satellite (GOES) Precipitation Index (Arkin and Meisner, 1987), the OLR Precipitation Index (OPI; Xie and Arkin, 1998), Spencer (Spencer, 1993), NOAA/NESDIS (Grody, 1991) and Chang (Wilheit *et al.*, 1991). Data are available on a 2.5° × 2.5° grid as pentad values from 1979 to 2008; for analysis purposes these have been linearly interpolated to daily values.

Horizontal wind and vertical velocity data are taken from the NCEP–Department of Energy (DOE) reanalysis (Kanamitsu *et al.*, 2002). Data were used on a 2.5° × 2.5° grid with 12 vertical levels (1000 to 100 hPa) and covered the same period as was available for OLR (1979–2013).

The analysis in this article covers the months November to April when the SPCZ and SACZ are strongest. Anomalies were computed by removing the annual cycle from the data; the annual cycle was defined as the mean plus the first three (five for precipitation data) annual harmonics. To separate synoptic-scale variability from variability at longer time-scales, a 20-day high-pass Lanczos filter (Duchon, 1979) was used.

3. Patterns of variability

Time series of daily OLR anomalies are defined in the centre of the SPCZ (175.0–180.0°E, 15.0–10.0°S, small grey box in Figure 1(b)) and SACZ (50.0–45.0°W, 20.0–15.0°S). To assess the dominant modes of temporal variability in the SPCZ and SACZ, smoothed power spectra of these time series are shown in Figure 2. Smoothing is based on a $L = 31$ point running mean. A red-noise theoretical background spectrum is added in black, based on the assumption that the time series were generated by a first-order Markov process and using the lag-1 autocorrelation coefficient ($r = 0.69$ for SPCZ and $r = 0.72$ for SACZ) of the time series (Wilks, 2006). The 95% confidence interval (dashed black line) was calculated by a chi-squared test using $2L$ degrees of freedom.

*(US) National Oceanographic and Atmospheric Administration/National Environmental Satellite Data and Information System.

†(US) National Centers for Environmental Prediction/National Climate Research Center.

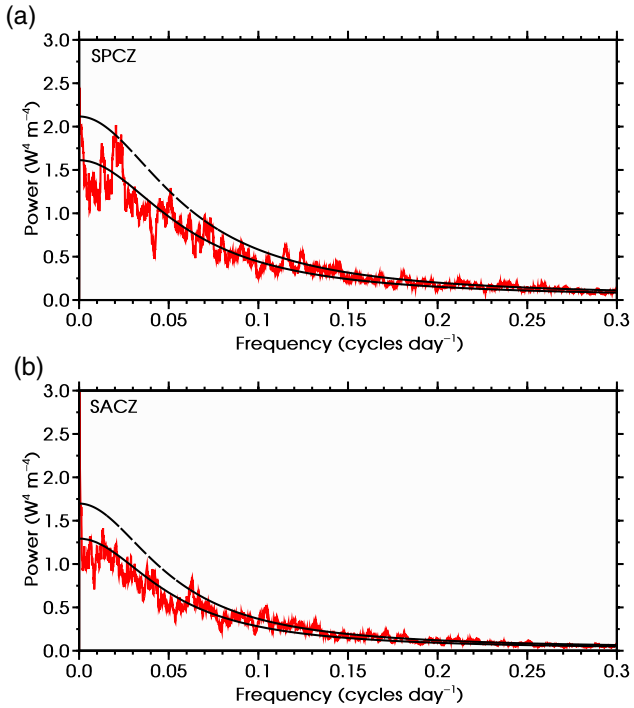

Figure 2. The 31-point smoothed power spectrum of daily OLR anomalies as a grey/red line averaged over a box in the centre of (a) the SPCZ (175.0–180.0°E, 15.0–10.0°S) and (b) the SACZ (50.0–45.0°W, 20.0–15.0°S). The locations are indicated in Figure 1(b). A red noise background spectrum and its 95% confidence limit are shown in black lines, solid and dashed respectively.

In the spectra of both the SPCZ and SACZ, there is a large peak at the lowest frequencies, corresponding to ENSO at interannual time-scales. At intraseasonal time-scales, variability is found only in the SPCZ, where there is a large peak at approximately 0.02 cycles day^{-1} or a 50 day period. This relates to the MJO, a 30–90 day coupled pattern in circulation and convection over the Indian and Pacific warm pool (Madden and Julian, 1971; Zhang, 2005) which has been shown to impact the SPCZ (Matthews *et al.*, 1996). Finally, at submonthly periods there are Rossby waves impacting both the SPCZ and the SACZ. This corresponds to peaks near 0.1 cycles day^{-1}, a 10 day period, and shorter time-scales.

Spatial patterns of variability in the SPCZ and SACZ are found by means of empirical orthogonal function (EOF) analysis. The EOFs are based on OLR anomalies over 34 austral summers (November to April, 1979/80 to 2012/13). The leading EOF patterns shown are significantly different from each other and following EOFs (North *et al.*, 1982). In Figure 3(a,b) the patterns associated with the first two EOFs of the SPCZ and the SACZ are shown. The EOFs are calculated separately for the SPCZ and the SACZ domains, but are plotted on the same figure for convenience.

For the SPCZ, all data within the box 150.0–220.0°E, 30.0°S–0.0° (black box in Figure 1(b)) are taken into account. The patterns found for the SPCZ variability are comparable to the patterns found by Matthews (2012), which were based on the same analysis but the data covered a shorter period of time. The first EOF accounts for 12.2% of the total variance and corresponds to what was named the 'southwestward shifted' mode. The pattern shows enhanced convection to the southwest of the mean convection axis and reduced convection to the northeast of the mean convection axis. The second EOF was described as the 'enhanced' mode. A similar pattern is found in this analysis (8.8% of the total variance), with enhanced convection on the mean convection axis and reduced convection on either side.

The patterns found over South America (SACZ region, box 80.0–20.0°W, 35.0°S–0.0°) are comparable to those of the SPCZ. The first EOF (10.1% of the total variance) shows enhanced convection to the southwest of the mean convection axis and reduced convection to the northeast, as described in the southwestward shifted mode. The second EOF (7.0% of the total

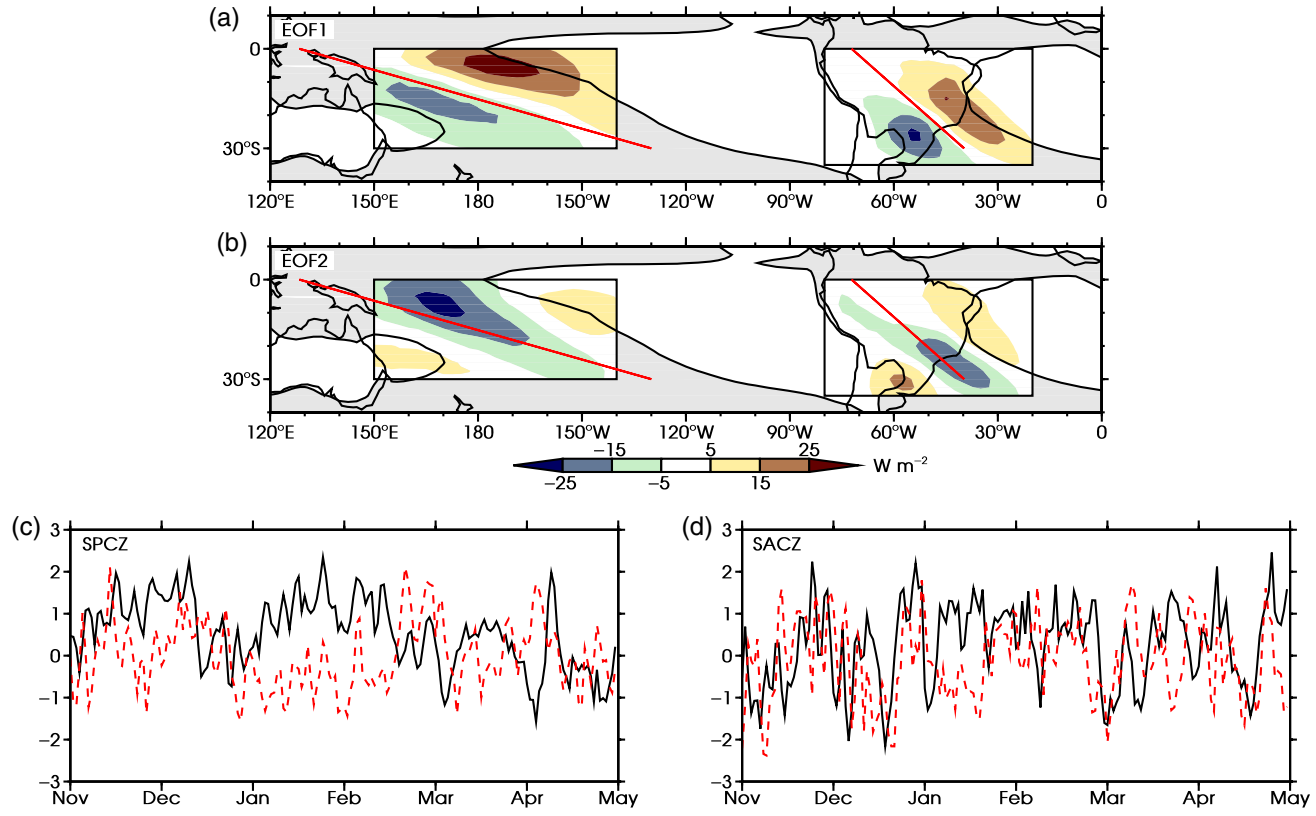

Figure 3. EOF patterns (a) 1 and (b) 2 (colour shading, W m^{-2}) in the rectangular boxes, overlayed on the November to April time mean OLR field (grey shading outside the rectangular boxes is < 250 W m^{-2}, as in Figure 1(b)). Grey/red diagonal lines indicate the positions of the mean convection axes of the SPCZ and the SACZ. Time series of the PCs associated with EOF 1 (black solid line) and EOF 2 (grey/red dashed line) during November–April 2000/01 for the (c) SPCZ and (d) SACZ.

variance) is the enhanced SACZ, with enhanced convection over the coastal and oceanic portion of the SACZ mean convection axis and reduced convection to the southwest and northeast. Note that in this case the largest variability is not located over the region of most intense rainfall, the Amazon, within the box.

Figure 3(c, d) show time series of the principal components (PCs) associated with the EOF patterns for the sample season of November 2000 to April 2001. These are daily amplitudes scaled to have standard deviation $\sigma = 1.0$. In both SPCZ and SACZ, the dominant mode of variability is on short, synoptic time-scales. Variability on intraseasonal time-scales is only visible in the SPCZ region as was concluded from the power spectra earlier. Lagged correlations between the time series of PC 1 and PC 2 in the SPCZ (calculated over all years) do not exceed $r = 0.02$ for lags up to a week. This is not significant at a $p = 95\%$ level according to the Pearson correlation coefficient statistical test. Therefore there is no evidence of a phase relationship between the patterns of EOF 1 and EOF 2, i.e. the southwestward shifted SPCZ mode does not develop into the enhanced SPCZ mode. For the SACZ there are significant cross-correlations from PC 1 to PC 2. For lags of 1–3 days, these are $r = 0.320$, 0.271 and 0.130 respectively. This indicates that the OLR anomalies propagate towards the northeast, as the southwestward shifted mode develops into the enhanced mode. Hence, both the SPCZ and SACZ experience variability at submonthly periods associated with Rossby wave activity. The spatial patterns associated with this variability are comparable for both regions, with respectively a southwestward shifted mode and an enhanced mode for EOFs 1 and 2. For the SPCZ these are similar to the patterns found in earlier analysis (Matthews, 2012).

Even though the variability patterns for the SPCZ and SACZ are similar, the temporal evolution is fundamentally different. In the SPCZ there is no evidence of propagation from EOF 1 to EOF 2. In the SACZ, significant lagged correlations are found from the time series of EOF 1 to EOF 2. The OLR anomalies of the southwestward shifted SACZ mode propagate northeastward in about 1–2 days to form the enhanced mode. In the next section these differences in temporal evolution will be discussed in more detail.

4. Wave propagation

Events of the southwestward shifted SPCZ and SACZ modes are investigated by means of composite analysis. A 'convective event' is defined when two criteria are met:

1. PC 1 $>1.0\,\sigma$; and
2. PC 1 is a maximum relative to 5 days before and 5 days after the event.

In total, 204 months were taken into account (November–April, 1979/80 to 2012/13). In this period there were 197 SPCZ convective events and 361 SACZ convective events based on the above criteria. Composites were computed by taking the mean of a field over all event days.

Figure 4(a) shows the SPCZ composites of OLR, 200 hPa vorticity and 200 hPa wind anomalies; negative OLR anomalies (enhanced convection) lie to the southwest of the mean convection axis and positive OLR anomalies (reduced convection) to the northeast. More enhanced convection is found over the Maritime Continent. The vorticity anomalies form a wave-like structure of cyclones (negative anomalies in the Southern Hemisphere) and anticyclones (positive anomalies). This is the Rossby wave train propagating from the subtropical jet stream towards the equatorial westerly duct which has been related to transient convection in the SPCZ (e.g Kiladis and Weickmann, 1992a; Widlansky *et al.*, 2011). Deep anomalous convection is found southwest of the mean convection axis, in the same location as the poleward, ascending flow ahead of a cyclonic anomaly. Northeast of the mean convection axis, equatorward descending flow ahead of an anticyclonic anomaly coincides with reduced convection. The precipitation anomalies associated with this pattern (not shown) are $+5.3\,\mathrm{mm\,day^{-1}}$ southwest of the mean convection axis and $-6.3\,\mathrm{mm\,day^{-1}}$ northeast of the mean convection axis.

Over South America the composite mean shows a similar combination of events (Figure 4(b)). A Rossby wave train propagates from the Pacific towards the Atlantic westerly duct, with vorticity anomalies that are stronger than in the SPCZ region (note the different red contour intervals in the figures). Ahead of the cyclonic vorticity anomaly, poleward wind is associated

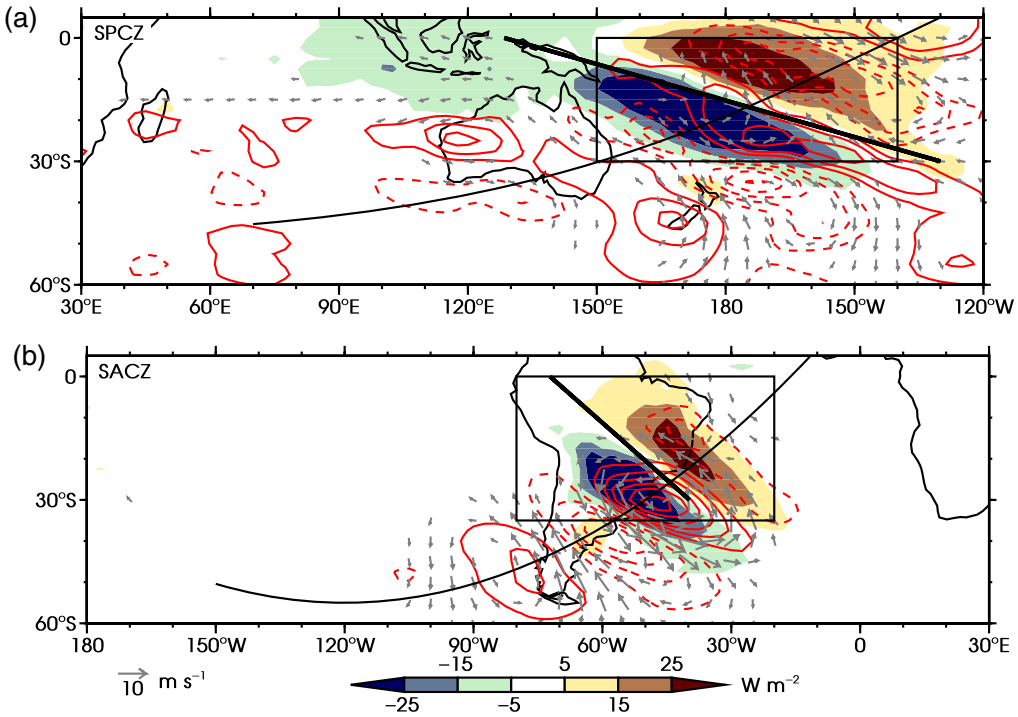

Figure 4. Composite anomalies of OLR (colour shading, $\mathrm{W\,m^{-2}}$), 200 hPa vorticity (grey/red contours, with 3×10^{-6} $\mathrm{s^{-1}}$ contour interval for (a) SPCZ and 6×10^{-6} $\mathrm{s^{-1}}$ for (b) SACZ, with zero contour omitted and negative contours dashed) and 200 hPa wind (vectors, $\mathrm{m\,s^{-1}}$, reference vector bottom left). The rectangle indicates the EOF region, the bold diagonal line the mean convection axis and the curved line an approximate wave propagation path.

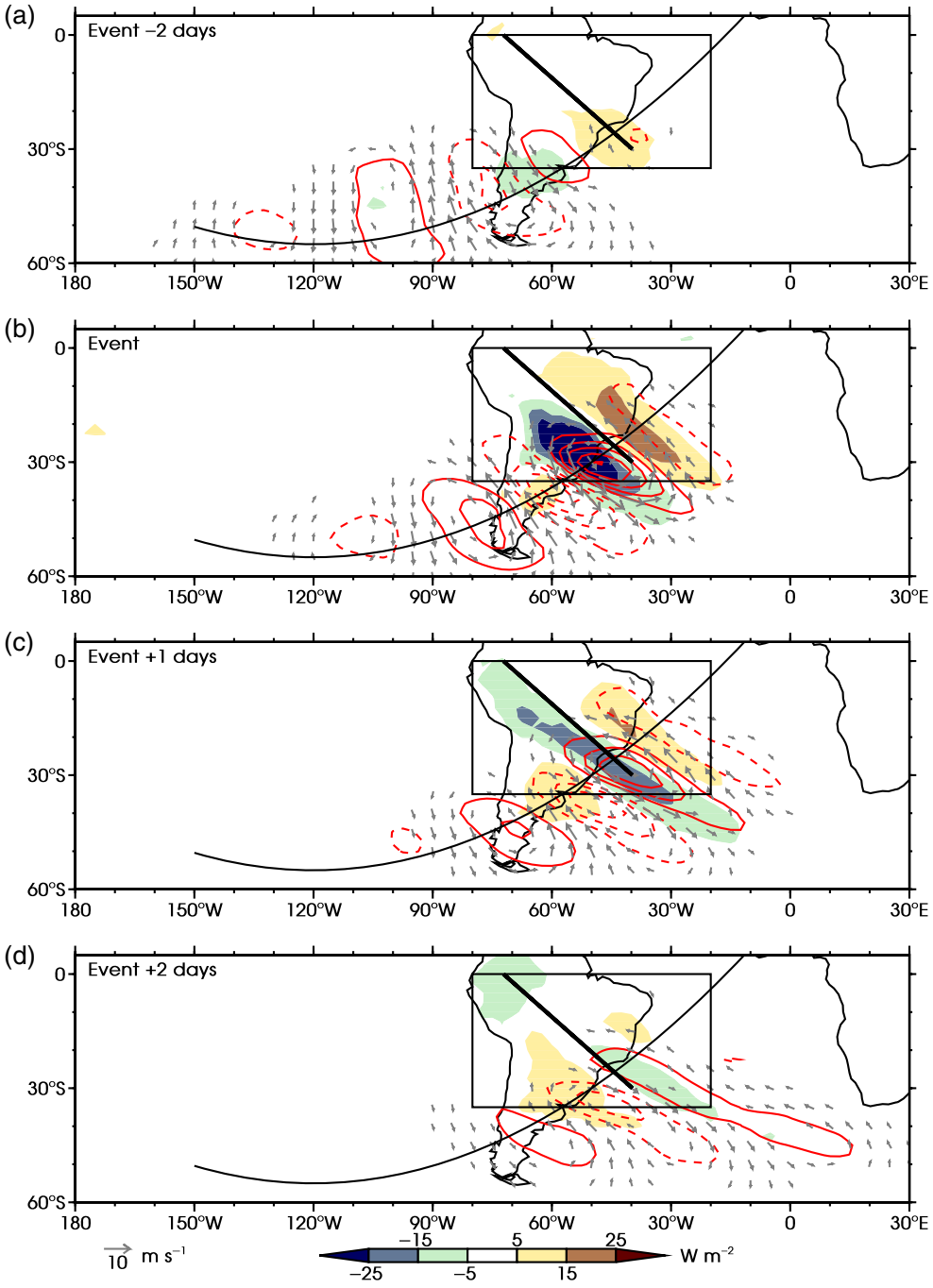

Figure 5. As Figure 4(b), but now lagged composites of 20 day high-pass filtered data, for time lags (a) event −2 days, (b) event, (c) event +1 day and (d) event +2 days.

with convection southwest of the mean convection axis. To the northeast and southwest of this region, anticyclonic vorticity centres and equatorward flow weaken convection. The associated precipitation anomalies are weaker than in the SPCZ region: in the enhanced convection an additional 2.4 mm day^{-1} of precipitation is generated, and the reduced convection decreases precipitation by 2.3 mm day^{-1}. This is despite similar sized OLR anomalies and is because mean precipitation in the SACZ is less than in the SPCZ (Figure 1(a)).

In the next two sections the SPCZ and SACZ will be discussed seperately. Analysis has shown the mechanism forcing the SACZ is simpler than the mechanism for the SPCZ, therefore the SACZ will be discussed first. Based on the lagged composite analysis, the temporal evolution of the equatorward propagating wave and the convection will be investigated. To separate the synoptic-scale variability of interest from variability at longer time-scales (e.g. MJO and ENSO), all subsequent data have been high-pass filtered before the composites are computed. Section 2 gives details.

5. A framework for diagonal SACZ development

5.1. *Observational overview*

Lagged composites of the days before and after the selected convective events give information on the temporal evolution of the wave train and convection anomalies (Figure 5). The Rossby wave train in the SACZ region can be tracked back into the central Pacific Ocean. In the days leading up to the convective event, quasi-circular vorticity anomalies propagate eastward. The vorticity anomalies are refracted equatorwards toward the upper-tropospheric mean westerlies over the equatorial Atlantic (Figure 1(c)). In this process the circular vorticity centres are deformed and obtain a northwest–southeast diagonal orientation.

In front of the cyclonic anomaly, anomalous poleward wind is found. Following quasi-geostrophic dynamics, poleward wind is associated with ascent and reduced static stability. In the conditionally unstable tropical atmosphere, this gives rise to deep

convection starting 2 days before the main convective event. This region of enhanced convection (negative OLR anomaly) travels with the wave along the propagation path and remains ahead of the cyclone at all times, intensifying with time. The opposite mechanism gives reduced convection ahead of anticyclonic vorticity. On the day of the convective event (Figure 5(b)) the vorticity anomalies lie parallel to the mean SACZ convection axis. By design of the composites, the convection peaks at the event date southwest of the mean convection axis. The precipitation rate that day (not shown) is 1.1 mm day^{-1}. A day after the event, the convective anomaly is located at the mean convection axis and reflects the enhanced SACZ mode. This is in agreement with previously found cross-correlations between the PCs of EOFs 1 and 2 (section 3). At event +2 days the convection has weakened and now lies to the northeast of the mean convection axis, the pattern resembling a weak negative southwestward shifted mode.

5.2. *Development of the diagonal orientation from Rossby wave dynamics*

Rossby wave propagation from the Subtropics towards the Equator and coincident deformation of the vorticity centres is a core mechanism in the development of the diagonal band of convection forced along the SACZ. Over the central Pacific, the vorticity centres inititally have an approximately circular shape; a northwest–southeast orientation is subsequently developed during their travel eastward and equatorward (e.g. Figure 5(b)). Here, two different models are used to test possible mechanisms for this deformation. First, the role of simple horizontal advection by the mean background wind $(\overline{u},\overline{v})$ is determined. Thirty points in a circle around 105°W, 45°S form a circular patch that models a vorticity centre in the jet (Figure 6(a)). Vorticity is advected only; there is no refraction by a Rossby wave mechanism. The advection and changing location of the tracer in time has been computed by means of a fourth-order Runge–Kutta scheme with a time step of 60 s. The plotted daily location of the vorticity tracer shows that in time the circular shape does evolve into a diagonally orientated shape due to shear on the northern side of the jet. However there is no discernible equatorward propagation due to the weak meridional wind.

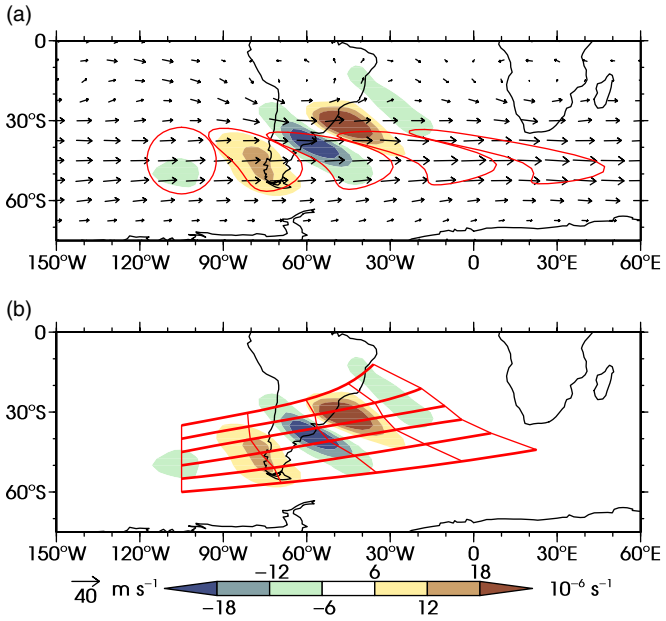

Figure 6. Two different wave propagation models for the SACZ. (a) Horizontal advection of a tracer by the 200 hPa November–April mean wind, with tracer positions for consecutive days in grey/red contours, and wind (vectors, m s^{-1}, reference vector bottom left). (b) Rossby ray propagation for the SACZ on the 200 hPa November–April mean wind, bolder grey/red lines show ray paths, thinner grey/red lines connect these at daily intervals. Vorticity anomalies are as in Figure 5(b) in colour shading (s^{-1}).

The second model demonstrates the role of non-divergent barotropic Rossby wave dynamics. The ray-tracing technique of Karoly (1983) for low-frequency Rossby waves is applied; scale separation between waves and mean flow is assumed. Rossby waves with initial zonal wavenumber $k_0 = 1.2 \times 10^{-6}$ m^{-1} and meridional wavenumber $l_0 = 6.9 \times 10^{-7}$ m^{-1} are initiated at $X_0 = 105°$W and six different latitudes across the jet between 35 and 60°S (Figure 6(b)). The change of the ray position and wavenumbers are integrated forward in time by the same Runge–Kutta scheme as in the first model. From their initial position, the Rossby rays take about 2 days to reach the SACZ area; during this time they become aligned with the vorticity centres that were found in the composite analysis. In contrast to the advection-only model, the meridional movement is strong enough to show clear equatorward propagation of the rays initiated on the northern edge of the jet. Once convection is triggered, the non-divergent dry model becomes a less valid description of the situation. However, during the approach to the SACZ region, the Rossby waves are dry and as a first approximation this simple model does show that barotropic Rossby wave dynamics can create the elongated, northwest–southeast oriented vorticity anomalies and equatorward propagation that lead to SACZ convection.

5.3. *Vertical structure*

Although barotropic non-divergent Rossby wave circulations can account for the diagonal orientation of the vorticity anomalies that force the SACZ, the baroclinic component of these circulations and their associated vertical motion then leads to triggering of convection. The vertical structure of the wave train is shown in Figure 7(a), which shows a section along the approximate wave path at the day of the event (curved black line in Figure 5(b)). The vorticity anomalies are strongest at 200 hPa and extend down to the surface in the SACZ region (the vertical line denotes the position of the mean convection axis). The pressure velocity anomalies are approximately in quadrature with the vorticity anomalies. Rising motions are found ahead of the cyclonic anomaly west of the mean convection axis, and descending motions in front of anticyclonic anomalies east of the mean convection axis. The strong rising motion is accompanied by convergence in the lower troposphere and divergence in the upper troposphere. The anticyclones up- and downstream of the cyclone are weaker but do give downward motion. Therefore convection is inhibited and upper-level convergence is found ahead of those.

The temporal development of the wave train and the associated convection anomaly along the curved propagation path is shown in a Hovmöller diagram (Figure 7(b)). Grey dashed lines indicate an approximate group velocity based on the Rossby ray-tracing results. The main region of vorticity activity lies within this group velocity envelope, consistent with the wave being governed by Rossby wave dynamics. The effects of phase and group velocity are visible. The leading edge of the wave packet propagates at the greater group velocity of approximately 29 m s^{-1} (dashed grey line in Figure 7(b) passing through 100°W, lag −5 days). Individual vorticity anomalies are initiated at this leading edge, e.g. the anticyclonic positive vorticity anomaly that begins around 110°W, lag −5 days (yellow shading). These vorticity anomalies propagate at the slower phase speed of approximately 7 m s^{-1}, increasing in amplitude as the centre of the energy envelope that defines the wave packet passes through them. Finally the trailing edge of the wave packet passes through, also at the group velocity of 29 m s^{-1}. At this point, the individual vorticity anomalies decay (around 10°W, lag +2 days for the positive vorticity anomaly) and eventually disappear.

Two days before the event, the cyclonic anomaly triggers convection. Together, the vorticity and convection anomaly propagate onwards. Two days after the event both anomalies weaken and the convective anomaly disappears.

A hypothesis of a possible link between wave propagation and the convection triggered by the wave was proposed in

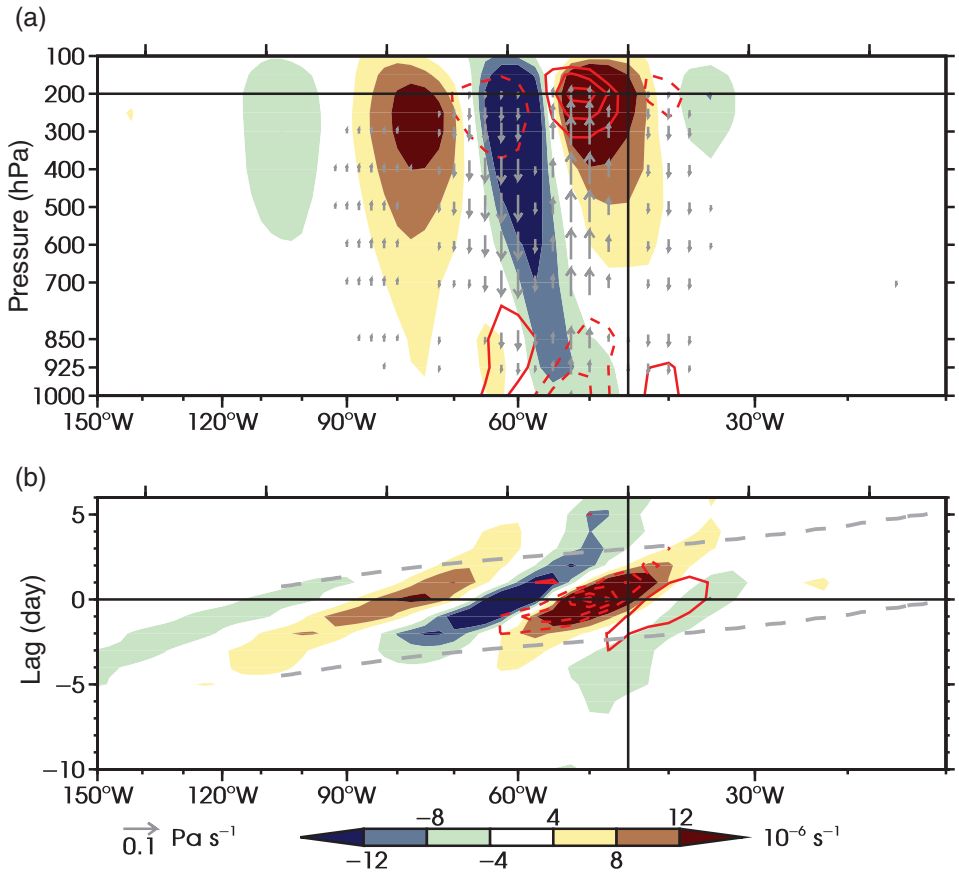

Figure 7. (a) Vertical cross-section of anomalies at the SACZ convective event along the curved propagation path (curved line in Figure 5(b)), vorticity (colour shading, s^{-1}), divergence (grey/red contours, 2×10^{-6} s^{-1} contour interval, zero contour omitted, negative contours dashed) and pressure velocity (vectors, Pa s^{-1}, reference vector bottom left). (b) Hovmöller diagram of lagged composite anomalies along the curved propagation path in the SACZ; 200 hPa vorticity (colour shading, s^{-1}) and OLR (grey/red contours, 10 W m^{-2} contour interval, zero contour omitted, negative contours dashed). Grey dashed lines indicate an approximate group wave speed, taken from Figure 6(b). All data are 20 day high-pass filtered. Horizontal axes are irregular longitude (bottom) or regular distance (top, 2000 km intervals) along the path. Vertical line indicates the position of the mean SACZ convection axis.

Matthews (2012): ascent in the Rossby wave triggers convection and precipitation. The diabatic heating released is substantial and enhances the ascent and upper-level divergence (Figure 7(a)). Divergence is a source of anticyclonic vorticity. As discussed before, the convection signal is in quadrature with the vorticity anomalies in the wave, with enhanced convection ahead of a cyclonic anomaly. The eastward propagating cyclone that triggered convection therefore encounters the generated anticyclonic vorticity when it moves along the wave path. The relative size of these two opposite vorticity terms ultimately determines whether or not the Rossby wave propagation can continue downstream of the triggered convection.

5.4. *Vorticity budget*

A quantitative analysis of the size of the different vorticity influences is needed to find the strength of the proposed negative feedback between wave dynamics and diabatic heating. Therefore all terms in the vorticity equation have been computed:

$$\underbrace{\frac{\partial \zeta}{\partial t}}_{\mathrm{I}} = \underbrace{-u\frac{\partial \zeta}{\partial x} - v\frac{\partial \zeta}{\partial y}}_{\mathrm{II}} \underbrace{-\omega\frac{\partial \zeta}{\partial p}}_{\mathrm{III}} \underbrace{-fD - \zeta D}_{\mathrm{IV}} \underbrace{-\beta v}_{\mathrm{V}} \underbrace{-\frac{\partial \omega}{\partial x}\frac{\partial v}{\partial p} + \frac{\partial \omega}{\partial y}\frac{\partial u}{\partial p}}_{\mathrm{VI}}, \quad (2)$$

where x and y are horizontal axes in the eastward and northward directions, respectively, p is pressure, u, v and ω are velocity components, and $\beta = \mathrm{d}f/\mathrm{d}y$ is the northward gradient of planetary vorticity (Holton, 2004, p. 103). The relative vorticity tendency (term I) is the result of the sum of the effects of horizontal (term II) and vertical (term III) advection of relative vorticity, vortex stretching (term IV), meridional advection of planetary vorticity (term V) and the tilting and twisting terms (term VI). Using 6 h NCEP–DOE reanalysis data at three levels (150, 200, 250 hPa), all terms in the vorticity equation have been computed at the 200 hPa level. Partial derivatives in time and pressure have been computed using centred differences. The residual balance from this computation is smaller than the main terms of interest and does not show a large-scale pattern. For reference, the residual will be plotted alongside the other terms.

In Figure 8 composites of the separate vorticity budget terms are shown for the day of the convective event. The budget is dominated by the horizontal advection terms and the vortex stretching terms. Horizontal advection (term II) of the wave pattern by both transient and background winds is the driving force for forward movement. The signal of horizontal advection is in quadrature with the wave pattern. Total horizontal advection of the cyclonic anomaly is partly balanced by the vortex stretching term (term IV) which has its maximum ahead of the cyclone where convection is triggered. This is the location of rising motion, enhanced convection and upper-level divergence forced by the wave (Figure 7(a)). The divergent outflow of air in the upper troposphere is a source of anticyclonic vorticity. The vorticity tendency is in quadrature with the vorticity pattern (quarter cycle ahead of the vorticity anomaly), resulting in continued propagation of the wave pattern.

The same composite analysis has been done for the enhanced SACZ mode (EOF 2, 397 selected events). The interaction between transient Rossby waves and convection is similar. The SACZ in its climatological position can be seen as the sum of all individual southwestward shifted and enhanced SACZ events. The atmospheric basic state gives rise to the equatorward refraction

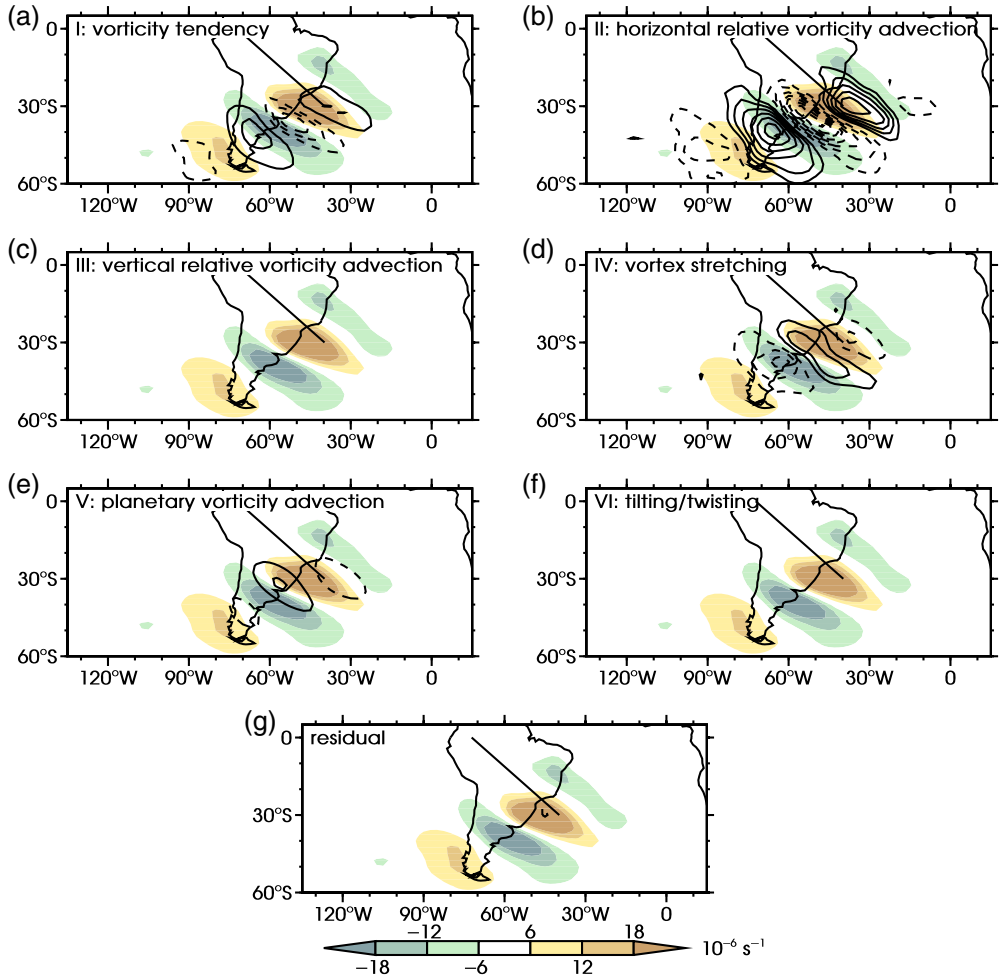

Figure 8. Composites of all terms in the full vorticity budget (Eq. (2)) for the SACZ at 200 hPa (contours, interval 1 $\times 10^{-5}$ s^{-1} day^{-1}, negative contours dashed, zero contour omitted): (a) term I, (b) term II, (c) term III, (d) term IV, (e) term V, (f) term VI and (g) the residual. Vorticity anomalies (colour shading, s^{-1}) as in Figure 4(b) are superimposed.

of Rossby waves that eventually leads to diagonal bands of deep convection and precipitation.

6. A framework for diagonal SPCZ development

A similar analysis, as undertaken for the SACZ, is presented here for the SPCZ. In Figure 9 lagged composites of the propagating wave and convection anomalies are shown. A wave train can be tracked to originate in the Indian Ocean. The vorticity anomalies are refracted equatorwards toward the upper-tropospheric mean westerlies over the equatorial Pacific (Figure 1(c)). As was found in the SACZ, originally quasi-circular vorticity centres get elongated in the northwest–southeast direction. On the day of the convective event, the vorticity centres lie parallel to the mean SPCZ convection axis. Ahead of the cyclonic anomaly, poleward ascending wind triggers deep convection in the tropical conditionally unstable atmosphere. The anomalous precipitation from this deep convection is a maximum at +1.9 mm day^{-1}. Northeast of the mean convection axis, a combination of anticyclonic vorticity and equatorward descending flow results in a diagonal band of reduced convection. Two days after the event, the OLR anomalies have mostly vanished. The wave train has not propagated further equatorward, and downstream of the SPCZ region the vorticity anomalies have disappeared. This is in contrast to the SACZ region where the convective anomalies travelled with the wave train and passed over the mean convection axis.

In the unfiltered composite of the SPCZ (Figure 4(a)) there is enhanced convection over the Maritime Continent. This signal has disappeared (Figure 9(c)) in the composites using 20 day high-pass filtered data because it is forced at longer time-scales than the synoptic time-scales at which the diagonal SPCZ convection is forced.

As was done for the SACZ, the role of horizontal advection in the wave propagation is investigated by means of a simple model. A circular patch centred around 50°E, 45°S is advected by the November–April mean 200 hPa wind (Figure 10(a)). As observed in the composites (Figure 9(b)), the originally circular patch deforms and becomes elongated in the northwest–southeast direction. However, the observed equatorward propagation is not found.

This equatorward refraction is found when non-divergent barotropic Rossby wave dynamics are added to the model (Figure 10(b)). Rossby rays starting at 50°E, across seven different latitudes (30–60°S) with initial wavenumbers $k_0 = 1.2 \times 10^{-6}$ m^{-1} and $l_0 = 4.4 \times 10^{-7}$ m^{-1} take about 4 days to propagate to the SPCZ region and acquire the diagonal orientation found in the composite analysis. The ray tracing is stopped there, as this is where the Rossby wave in the composites loses coherence. The mechanisms involved in setting up the diagonal vorticity centres at the base of the diagonal convection are similar for the SACZ and the SPCZ. Vorticity centres become elongated with a northwest–southeast tilt due to the zonal wind shear at the equatorward flank of the jet stream. Equatorward propagation is primarily due to refraction.

The vertical section (Figure 11(a)) through the wave shows a similar structure to the SACZ wave. The wave train of cyclones and anticyclones is strongest at about 200 hPa, with the main cyclonic anomaly reaching to the surface. Ahead of the cyclone there are strong rising motions which are accompanied by convergence at the surface and divergence aloft. The anticyclone upstream of the cyclone gives downward motion, therefore convection is

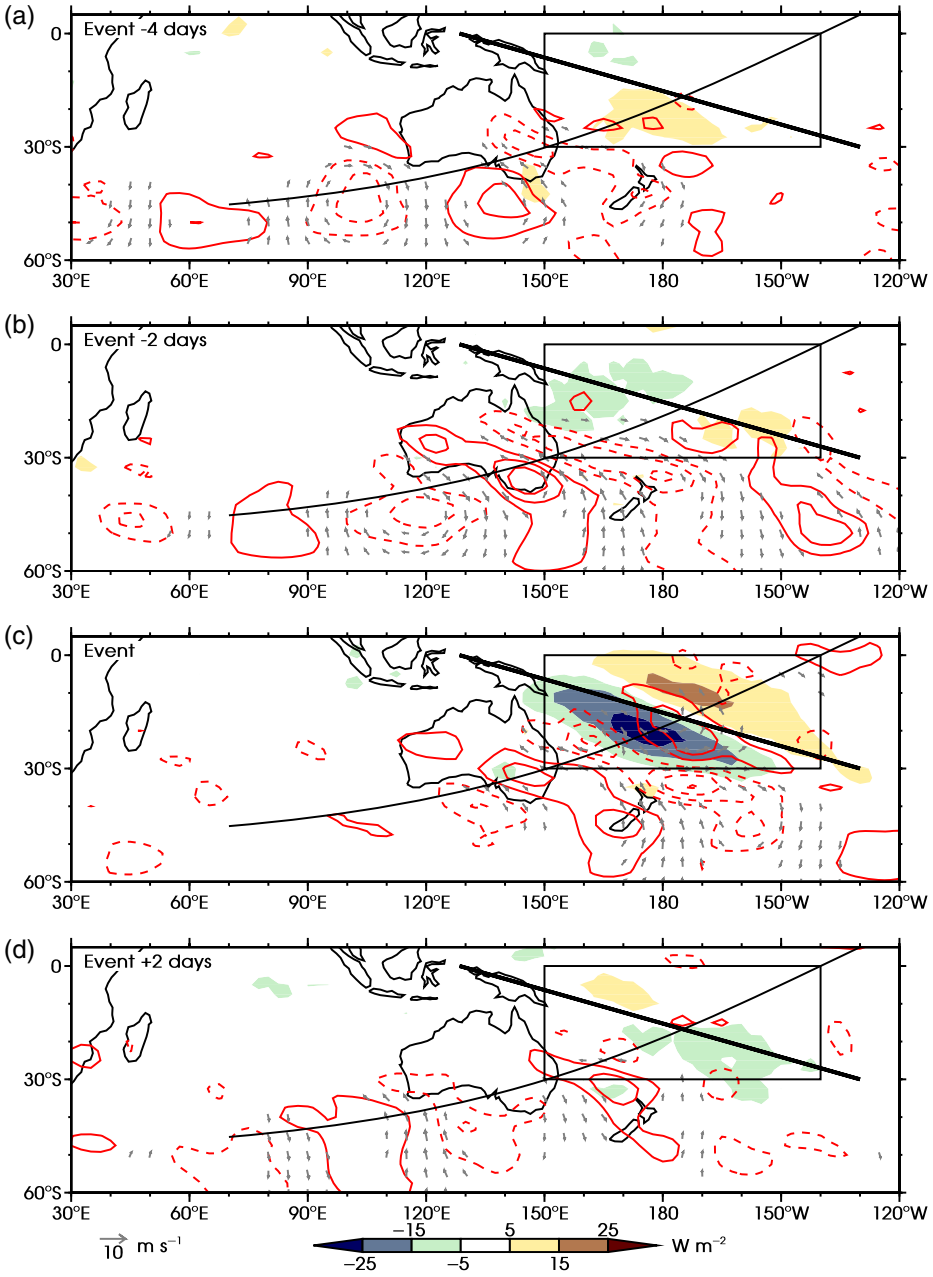

Figure 9. As Figure 4(a), but now lagged composites of 20 day high-pass filtered data for time lags (a) event −4 days, (b) event −2 days, (c) event and (d) event +2 days.

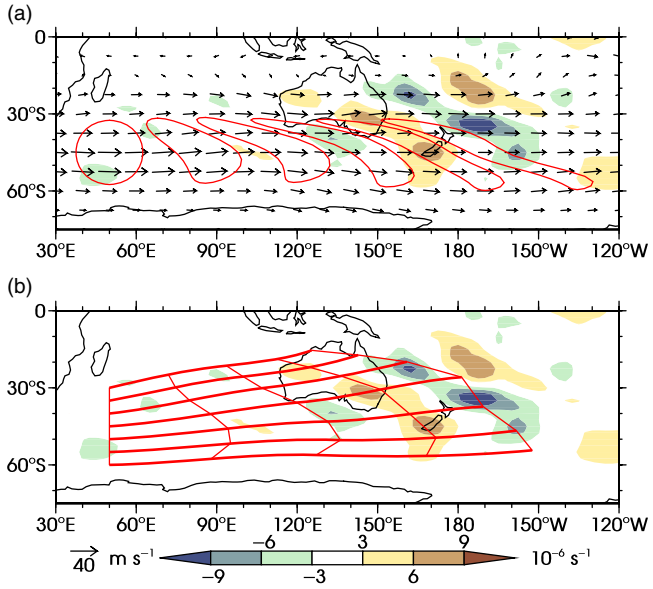

Figure 10. As Figure 6 but now for SPCZ.

inhibited and upper-level convergence is found ahead of this anticyclone.

The propagation of vorticity and OLR anomalies are shown in a Hovmöller diagram (Figure 11(b)). West of the mean convection axis and before the convective event there is clear eastward propagation of the vorticity anomalies at approximately 500 km day^{-1} ≈ 5.8 m s^{-1}. The grey dashed diagonal lines show the approximate group velocity which is derived from the ray paths in Figure 10(b). Again, this energy envelope confines the wave packet. Near the mean convection axis, short-lived OLR anomalies appear, with enhanced convection ahead of the cyclonic vorticity centre and reduced convection ahead of the anticyclonic vorticity. These convective anomalies do not propagate along the wave path and the vorticity anomalies do not propagate downstream of the mean SPCZ convection axis. Instead, the Rossby wave loses coherence and decays at the convective event.

It seems the SPCZ area forms a barrier for the Rossby waves; this is fundamentally different from the wave propagation we found in the SACZ area. The feedback between wave propagation and diabatic heating from triggered deep convection must therefore be different. Quantitative evidence for the relative strength of the negative feedback is provided by the computation of the vorticity

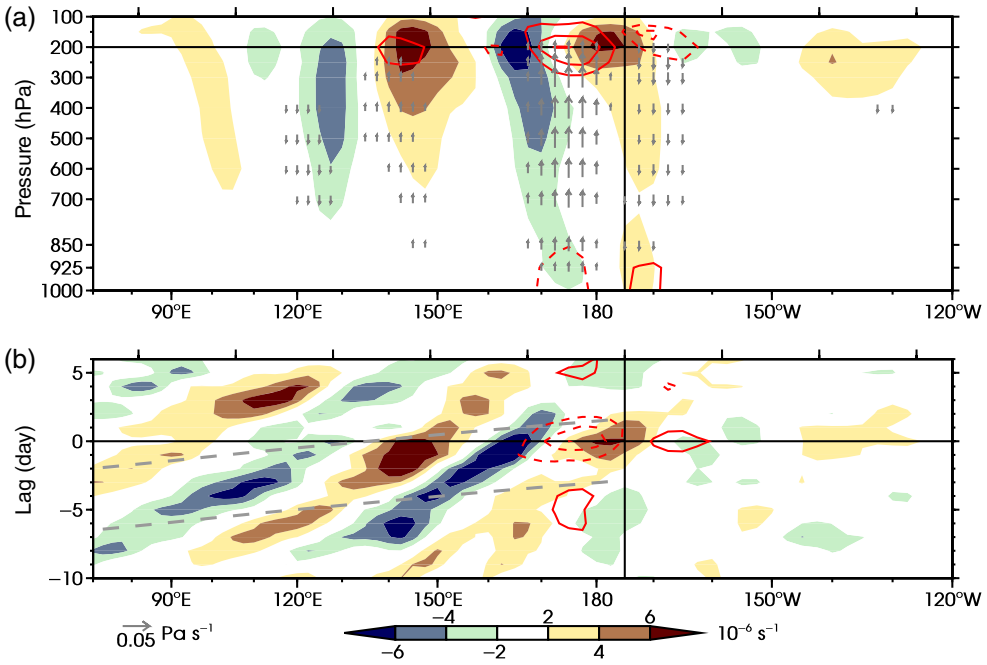

Figure 11. As Figure 7, but now for the curved propagation path of the SPCZ (Figure 9). Notice different vector scaling, colour scale and contour interval for divergence (1×10^{-6} s^{-1}).

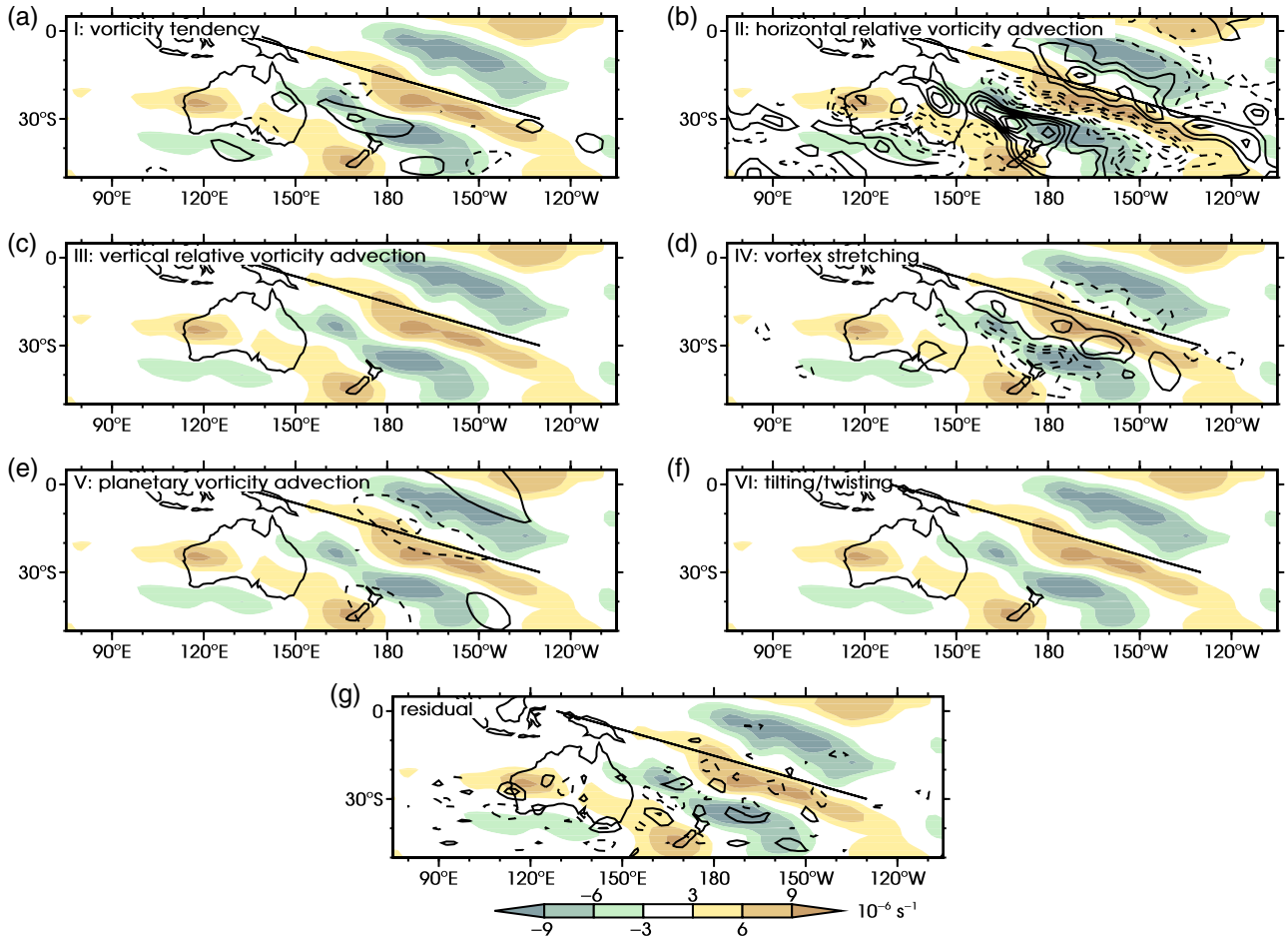

Figure 12. As Figure 8 but now for the SPCZ. Note different contour interval (0.5×10^{-5} s^{-1} day^{-1}).

budget (Eq. (2)). In Figure 12 all separate terms and the residual are plotted for the day of the convective event. In the SACZ region, horizontal advection of relative vorticity was dominant and forced continued propagation of the wave. Also in the SPCZ region the horizontal advection term (term II) shows northeastward propagation of the wave pattern; ahead of the cyclone negative vorticity tendency is found. However, vortex stretching (term IV) largely cancels this propagation. The anticyclonic tendency ahead of the cyclone relates to upper-troposheric divergence found ahead of the cyclonic anomaly (Figure 11(a)). The sum of the two effects, the vorticity tendency, is close to zero so the cyclone does not move. This is the key SACZ/SPCZ difference. Meanwhile, the upstream anticyclonic anomaly does move forward into the stationary cyclonic anomaly. The negative feedback between Rossby wave and transient convection stops and dissipates the Rossby wave.

As in the SACZ region, the diagonal convection band of the SPCZ is forced by equatorward propagating Rossby waves originating in the southern jet. In contrast to the SACZ, the latent heat released in the convection is strong enough to stop the wave propagation. The vorticity centres in the SPCZ wave train are much weaker than those of the wave train in the SACZ region. As a result, the forced poleward wind and upward motion are also weaker in the SPCZ. However, the SPCZ precipitation that is induced is, in contrast, greater than in the SACZ. The additional latent heat from condensation is therefore relatively more important and the additional upper-tropospheric divergence and anticyclonic vorticity tendency it generates is strong enough to dissipate the wave *in situ*. This is consistent with the non-significant cross-correlations that were found between the PC time series of EOF 1 and 2 for the SPCZ.

7. Discussion

Observation-based data products have been used to investigate patterns of variability in the SPCZ and SACZ regions; the focus has been on variability at synoptic time-scales. Two spatial patterns of variability have been found in both the SPCZ and SACZ regions. The main mode is a 'southwestward shifted' convection pattern, the second mode is an 'enhanced' convection pattern. The EOF patterns and associated PC time series have been used for composite analysis to find the temporal development of these modes.

The chain of events leading to a diagonal rainfall band in the SPCZ region is shown in schematic form in Figure 13. A wave train originating from the southern subtropical jet refracts northeastward towards the east Pacific equatorial westerly duct (1). The originally quasi-circular vorticity anomalies get an elongated diagonal structure due to shear on the northern edge of the jet. Ray-tracing techniques have shown dry non-divergent barotropic Rossby dynamics provide the equatorward propagation, as has been suggested by Hoskins and Ambrizzi (1993). Ahead of a cyclonic vorticity anomaly, poleward wind ascends and triggers convection (2). This convection anomaly has a northwest–southeast orientation similar to the vorticity anomalies, parallel to the mean convection axis. The mechanism is similar to that which causes transient convection in the ITCZ

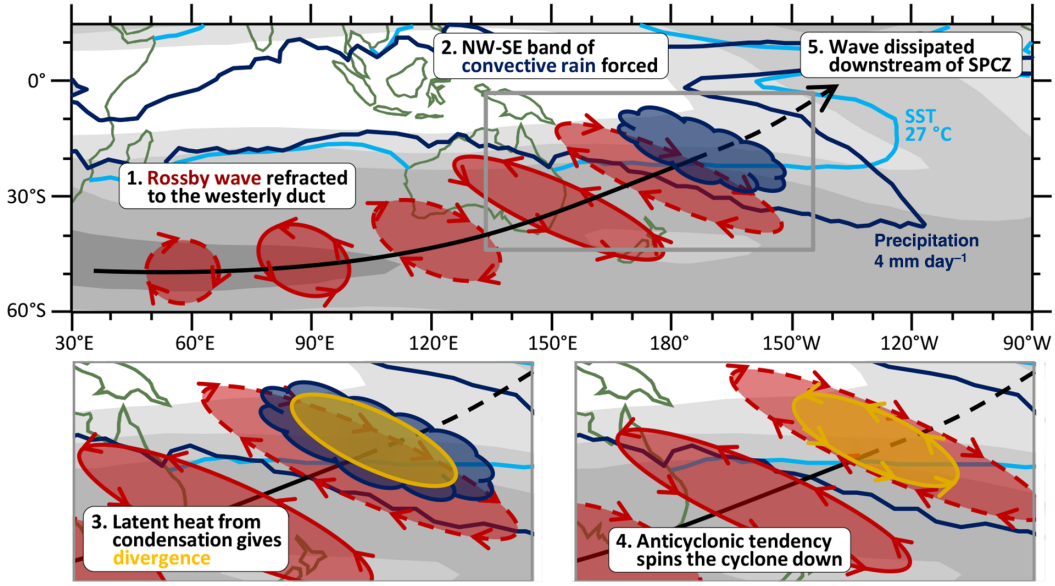

Figure 13. Schematic of mechanism for the development of a diagonal SPCZ. A Rossby wave train from the southern tropical jet is refracted towards the equatorial Pacific westerly duct (1). Originally quasi-circular vorticity centres deform to have a northwest–southeast elongation. Ahead of a cyclonic vorticity anomaly, poleward wind is associated with destabilisation and ascending motions that trigger deep convection in a diagonal band (2). Latent heat from condensation gives additional ascent and upper-tropospheric divergence (3). This leads to an anticyclonic vorticity tendency through vortex stretching ahead of the cyclone, however continued horizontal propagation of the cyclone brings it over this area and spins the cyclone down (4). The cyclone is dissipated *in situ* and hence Rossby wave propagation stops in the SPCZ area (5).

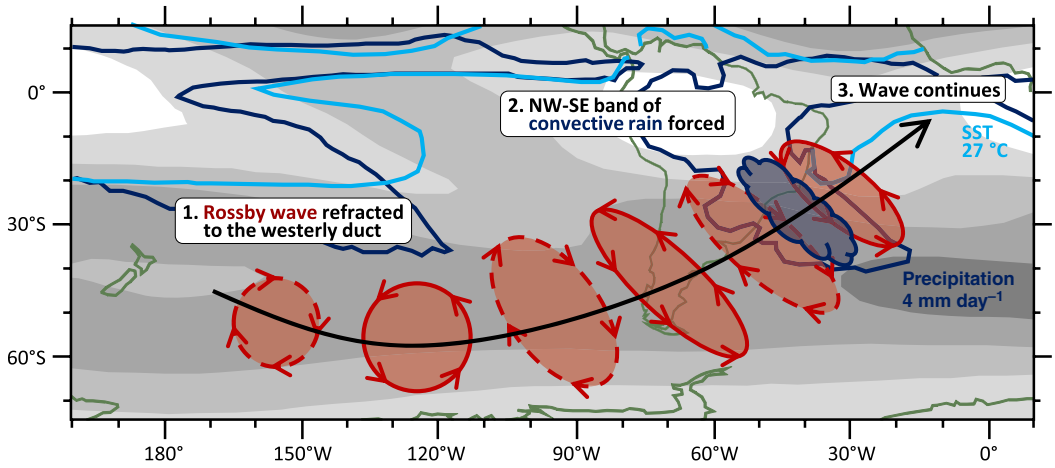

Figure 14. Schematic of mechanism for the development of a diagonal SACZ. A Rossby wave train from the central South Pacific is refracted towards the equatorial Atlantic westerly duct (1). Originally quasi-circular vorticity centres deform to have a northwest–southeast elongation. Ahead of a cyclonic vorticity anomaly, poleward wind is associated with destabilisation and ascending motions that trigger deep convection in a diagonal band (2). Though latent heat from condensation gives additional ascent and upper-tropospheric divergence, the associated anticyclonic vorticity tendency is not strong enough to dissipate the wave. The Rossby wave therefore continues propagating equatorward after forcing convection (3).

during austral summer (Kiladis and Weickmann, 1992a, 1992b). Condensation and subsequent latent heat release in the convection force additional ascent and upper-tropospheric divergence (3). Through vortex stretching, this results in an anticyclonic vorticity tendency which acts to weaken the initial cyclonic anomaly (4). Depending on the strength of the negative feedback, the wave can propagate onwards or dissipate. The computation of a full vorticity budget allows for a quantitative analysis of the relative importance of different vorticity tendency terms in the propagation of the transient wave. In the SPCZ this has shown that the feedback is strong enough to dissipate the wave within a day and propagation stops in the SPCZ region (5). This is in agreement with the proposed hypothesis and scale analysis of Matthews (2012).

Figure 14 shows the mechanism for the development of the diagonal SACZ. Over South America a comparable wave train propagates equatorwards towards the Atlantic westerly duct (1). The same mechanisms that provided the northeast–southwest tilt and equatorward propagation in the SPCZ act here. A cyclone triggers diagonally oriented convection (2) and forces upper-level divergence, as was also the case in the SPCZ region. However, the vorticity budget calculations in this case show that the divergence forced by the wave is not strong enough to dissipate the wave *in situ*. The wave and convection therefore propagate past the mean convection axis (3). This is in agreement with the cross-correlations found between the PCs of the shifted and enhanced modes that were found in the SACZ only.

The existence of both the SPCZ and SACZ is due to the atmospheric basic state. Following the conceptual framework of Meehl *et al.* (2001), processes at longer time-scales and larger spatial scales, including ENSO and MJO, set the base state upon which the transient Rossby waves get refracted equatorward. The accumulated effect of individual waves and short-lived pulses of convection then feed back on to the mean state.

Acknowledgements

The CMAP, interpolated OLR and NCEP Reanalysis data were provided by the NOAA/OAR/ESRL PSD, Boulder, Colorado, USA, from their web site at http://www.cdc.noaa.gov/ (accessed 8 January 2015). The research presented in this article was carried out on the High Performance Computing Cluster supported by the Research Computing Service at the University of East Anglia. The authors would like to thank Ben Lintner and an anonymous reviewer for comments which helped to improve the manuscript.

References

Ambrizzi T, Hoskins BJ, Hsu H-H. 1995. Rossby wave propagation and teleconnection patterns in the austral winter. *J. Atmos. Sci.* **52**: 3661–3672.

Arkin PA, Meisner BN. 1987. The relationship between large-scale convective rainfall and cold cloud over the western hemisphere during 1982–1984. *Mon. Weather Rev.* **115**: 51–74.

Cai W, Lengaigne M, Borlace S, Collins M, Cowan T, McPhaden MJ, Timmermann A, Power S, Brown J, Menkes C, Ngari A, Vincent EM, Widlansky MJ. 2012. More extreme swings of the South Pacific Convergence Zone due to greenhouse warming. *Nature* **488**: 365–370.

Cook KH. 2000. The South Indian Convergence Zone and interannual rainfall variability over Southern Africa. *J. Clim.* **13**: 3789–3804.

Duchon CE. 1979. Lanczos filtering in one and two dimensions. *J. Appl. Meteorol.* **18**: 1016–1022.

Folland CK, Renwick JA, Salinger MJ, Mullan AB. 2002. Relative influences of the Interdecadal Pacific Oscillation and ENSO on the South Pacific Convergence Zone. *Geophys. Res. Lett.* **29**: 21-1–21-4. doi: 10.1029/2001GL014201.

Griffiths GM, Salinger MH, Leleu I. 2003. Trends in extreme daily rainfall across the South Pacific and relationship to the South Pacific Convergence Zone. *Int. J. Climatol.* **23**: 847–869.

Grody NC. 1991. Classification of snow cover and precipitation using the special sensor microwave imager. *J. Geophys. Res.* **96**: 7423–7435, doi: 10.1029/91JD00045.

Haffke C, Magnusdottir G. 2013. The South Pacific Convergence Zone in three decades of satellite images. *J. Geophys. Res.* **118**: 1–11, doi: 10.1002/jgrd.50838.

Holton JR. 2004. *An Introduction to Dynamical Meteorology* (4th edn). Elsevier Academic Press: Burlington, MA.

Hoskins BJ, Ambrizzi T. 1993. Rossby wave propagation on a realistic longitudinally varying flow. *J. Atmos. Sci.* **50**: 797–812.

Hubert LF. 1961. A subtropical convergence line of the South Pacific: A case study using meteorological satellite data. *J. Geophys. Res.* **66**: 1661–1671, doi: 10.1029/JZ066i003p00797.

Janowiak JE, Arkin PA. 1991. Rainfall variation in the tropics during 1986–1989, as estimated from observations of cloud-top temperature. *J. Geophys. Res.* **96**: 3359–3373, doi: 10.1029/90JD01856.

Kalnay E, Kanamitsu M, Kistler R, Collins W, Deaven D, Gandin L, Iredell M, Saha S, White G, Woollen J, Zhu Y, Leetmaa A, Reynolds R, Chelliah M, Ebisuzaki W, Higgins W, Janowiak J, Ropelewski KC, Mo C, Wang J, Jenne R, Joseph D. 1996. The NCEP/NCAR 40-year reanalysis project. *Bull. Am. Meteorol. Soc.* **77**: 437–473.

Kanamitsu M, Ebisuzaki W, Yang S-K, Hnilo JJ, Fiorino M, Potter GL. 2002. NCEP DOE AMIP-II reanalysis (R-2). *Bull. Am. Meteorol. Soc.* **83**: 1631–1643.

Karoly DJ. 1983. Rossby wave propagation in a barotropic atmosphere. *Dyn. Atmos. Oceans* **7**: 111–125.

Kiladis GN. 1998. Observations of Rossby waves linked to convection over the eastern tropical Pacific. *J. Atmos. Sci.* **55**: 321–339.

Kiladis GN, Weickmann KM. 1992a. Circulation anomalies associated with tropical convection during northern winter. *Mon. Weather Rev.* **120**: 1900–1923.

Kiladis GN, Weickmann KM. 1992b. Extratropical forcing of tropical Pacific convection during northern winter. *Mon. Weather Rev.* **120**: 1924–1938.

Kiladis GN, von Storch H, van Loon H. 1989. Origin of the South Pacific Convergence Zone. *J. Clim.* **2**: 1185–1195.

Kodama YM. 1992. Large-scale common features of subtropical precipitation zones (the Baiu Frontal Zone, the SPCZ, and the SACZ) Part I: Characteristics of subtropical frontal zones. *J. Meteorol. Soc. Jpn.* **70**: 813–836.

Kodama YM. 1993. Large-scale common features of subtropical convergence zones (the Baiu Frontal Zone, the SPCZ, and the SACZ) Part II: Conditions of the circulations for generating the STCZs. *J. Meteorol. Soc. Jpn.* **71**: 581–610.

Kumar VV, Deo RC, Ramachandran V. 2006. Total rain accumulation and rain-rate analysis for small tropical Pacific islands: A case study of Suva, Fiji. *Atmos. Sci. Lett.* **7**: 53–58.

Lau K-M, Chan PH. 1983. Short-term climate variability and atmospheric teleconnections from satellite-observed outgoing longwave radiation. I: Simultaneous relationships. *J. Atmos. Sci.* **40**: 2735–2750.

Liebmann B, Smith CA. 1996. Description of a complete (interpolated) outgoing longwave radiation dataset. *Bull. Am. Meteorol. Soc.* **77**: 1275–1277.

Liebmann B, Kiladis GN, Marengo JA, Ambrizzi T, Glick JD. 1999. Submonthly convective variability over South America and the South Atlantic convergence zone. *J. Clim.* **12**: 1877–1891.

Lintner BR, Neelin JD. 2008. Eastern margin variability of the South Pacific Convergence Zone. *Geophys. Res. Lett.* **35**: L16701, doi: 10.1029/2008GL034298.

Madden RA, Julian PR. 1971. Detection of a 40–50 day oscillation in the zonal wind in the tropical Pacific. *J. Atmos. Sci.* **28**: 702–708.

Matthews AJ. 2012. A multiscale framework for the origin and variability of the South Pacific Convergence Zone. *Q. J. R. Meteorol. Soc.* **138**: 1165–1178.

Matthews AJ, Hoskins BJ, Slingo JM, Blackburn M. 1996. Development of convection along the SPCZ within a Madden-Julian Oscillation. *Q. J. R. Meteorol. Soc.* **122**: 669–688.

Meehl GA, Lukas R, Kiladis GN, Weickmann KM, Matthews AJ, Wheeler M. 2001. A conceptual framework for time- and space-scale interactions in the climate system. *Clim. Dyn.* **17**: 753–775.

Murphy BF, Powerand SB, McGree S. 2014. The varied impacts of El Niño-Southern Oscillation on Pacific island climates. *J. Clim.* **27**: 4015–4036.

Nieto Ferreira R, Chao WC. 2013. Aqua-planet simulations of the formation of the South Atlantic convergence zone. *Int. J. Climatol.* **33**: 615–628.

Nieto Ferreira R, Rickenbach TM, Wright EA. 2011. The role of cold fronts in the onset of the monsoon season in the South Atlantic convergence zone. *Q. J. R. Meteorol. Soc.* **137**: 908–922.

North GR, Bell TL, Cahalan RF. 1982. Sampling errors in the estimation of empirical orthogonal functions. *Mon. Weather Rev.* **110**: 699–706.

Ortéga P, Guignes T. 2007. Lightning activity analyses with respect to the SPCZ location. *Geophys. Res. Lett.* **34**: L11807, doi: 10.1029/2007GL029730.

Robertson AW, Mechoso CR. 2000. Interannual and interdecadal variability of the South Atlantic Convergence Zone. *Mon. Weather Rev.* **128**: 2947–2957.

Rudolf B, Hauschild H, Rueth W, Schneider U. 1994. Terrestrial precipitation analysis: Operational method and required density of point measurements. *NATO ASI Ser.* **126**: 173–186.

Salby ML. 2012. *Physics of the Atmosphere and Climate* (1st edn). Cambridge University Press: New York, NY.

Salinger MJ, Renwick JA, Mullan AB. 2001. Interdecadal Pacific Oscillation and South Pacific climate. *Int. J. Climatol.* **21**: 1705–1721.

Spencer RW. 1993. Global oceanic precipitation from the MSU during 1979–1991 and comparisons to other climatologies. *J. Clim.* **6**: 1301–1326.

Streten NA. 1973. Some characteristics of satellite-observed bands of persistent cloudiness over the Southern Hemisphere. *Mon. Weather Rev.* **101**: 486–495.

Takahashi K, Battisti DS. 2007. Processes controlling the mean tropical Pacific precipitation pattern. Part II: The SPCZ and the southeast Pacific dry zone. *J. Clim.* **20**: 5696–5706.

Todd MC, Washington R, James T. 2003. Characteristics of summertime daily rainfall variability over South America and the South Atlantic convergence zone. *Meteorol. Atmos. Phys.* **83**: 89–108.

Trenberth KE. 1976. Spatial and temporal variations of the Southern Oscillation. *Q. J. R. Meteorol. Soc.* **102**: 639–653.

Vincent DG. 1994. The South Pacific Convergence Zone (SPCZ): A review. *Mon. Weather Rev.* **122**: 1949–1970.

Vincent EM, Lengaigne M, Menkes CE, Jourdain NC, Marchesiello P, Madec G. 2011. Interannual variability of the South Pacific Convergence Zone and implications for tropical cyclone genesis. *Clim. Dyn.* **36**: 1881–1896.

Webster PJ, Holton JR. 1982. Cross-equatorial response to middle-latitude forcing in a zonally varying basic state. *J. Atmos. Sci.* **39**: 722–733.

Widlansky MJ, Webster PJ, Hoyos CD. 2011. On the location and orientation of the South Pacific Convergence Zone. *Clim. Dyn.* **36**: 561–578.

Wilheit TT, Chang ATC, Chiu LS. 1991. Retrieval of the monthly rainfall indices from microwave radiometric measurements using probability distribution functions. *J. Atmos. Oceanic Technol.* **8**: 118–136.

Wilks DS. 2006. *Statistical Methods in the Atmospheric Sciences* (2nd edn). Elsevier Academic Press: Burlington, MA.

Xie P, Arkin PA. 1997. Global precipitation: A 17-year monthly analysis based on gauge observations, satellite estimates, and numerical model outputs. *Bull. Am. Meteorol. Soc.* **78**: 2539–2558.

Xie P, Arkin PA. 1998. Global montly precipitation extimates from satellite-observed outgoing longwave radiation. *J. Clim.* **11**: 137–164.

Yang G-Y, Hoskins BJ. 1996. Propagation of Rossby waves of non-zero frequency. *J. Atmos. Sci.* **53**: 2365–2378.

Zhang C. 2005. Madden–Julian Oscillation. *Rev. Geophys.* **43**: RG2003.

